Supporting Information

Highly Efficient Cooperative CO_2 Electroreduction to CH_4 on a Copper Cluster/C_{60} Hetero-Structured Catalyst

Yanlei Liang, [†,§] *Jun Wang,* [†,§] *Qiaolin Wang,* [†] *Zhiyuan Wang,* [Δ] *Xifan Chen,* [†] *Junzhong Wang,* [†] *Juan-Ding Xiao,* [†] *Zhengkun Yang,* [†,*] *Xiaoping Gao,* [‡,*] *Jia Yang* [†,*]

[†] Institutes of Physical Science and Information Technology, Anhui Graphene Carbon Fiber Materials Research Center, Anhui University, Hefei, Anhui 230601, China

[‡] School of New Energy, Ningbo University of Technology, Ningbo, Zhejiang 315336, China

[Δ] Henan Institute of Advanced Technology, Zhengzhou University, Zhengzhou 450001, China

[§] These authors contributed equally

* E-mail: yangzk@ustc.edu.cn, gaoxiaoping2014@foxmail.com, yj4368@ahu.edu.cn

DFT calculations: The DFT calculations were performed via Vienna *ab initio* simulation package (VASP)[1,2]. The ion-electron interaction was described with the projector-augmented plane-wave (PAW) method[3]. Exchange-correlation energy was expressed by Perdew-Burke-Ernzerhof (PBE) functional with the generalized gradient approximation (GGA)[4]. The 1,10-phenanthroline-Cu_{13}/C_{60} hetero-structured catalyst was modelled by constructing a cluster with 13 copper atoms connecting the1,10-phenanthroline on the C_{60} support. While the Cu_{13}/C_{60} catalyst was built by constructing a cluster with 13 copper atoms on the C_{60} support. The 1,10-phenanthroline-Cu_{13}/graphene sample was constructed by loading a cluster with 13 copper atoms connecting the 1,10-phenanthroline on the graphene support. To avoid the interlayer interaction, the vacuum layer of the samples was set to 15 Å. For geometry optimization, the cut-off energy was set to be 520 eV, and the Brillouin zone was sampled with the Gamma point. The systems were relaxed until the energy and force reached the convergence threshold of 10^{-5} eV and 0.02 eV/Å, respectively. We describe the van der Waals (vdW) interactions by utilizing the DFT-D3 method[5].

For the barriers of H_2O dissociation to H and OH intermediates on p-Cu_{13}/C_{60} and p-Cu_{13}/Graphene, we did free energy calculation for each point along the NEB[6] reaction path using VASP, so that the geometry of the transition state could change adiabatically as a function of applied potential. The VTST package[7] with climbing image nudged elastic band (CI-NEB)[8] was used to obtain the reaction pathway and transition states.

Gibbs free energies for each gaseous and adsorbed species were calculated at 298.15 K, according to the expression:

$$G = E_{DFT} + E_{ZPE} - TS \qquad (1)$$

where E_{DFT} is the electronic energy calculated with VASP, E_{ZPE} is the zero-point energy, and TS is the entropy contribution. Standard ideal gas methods were employed to compute E_{ZPE} and TS from temperature, pressure, and the calculated vibrational energies. For adsorbates, all 3*N* degrees of freedom were treated as frustrated harmonic vibrations with negligible contributions from the catalysts' surfaces. In the computational hydrogen electrode (CHE) model[9], each reaction step was treated as a simultaneous transfer of the proton-electron pair as a function of the applied potential. Thus, free energy changes relative to an initial state of gaseous CO_2 free above an empty surface can be represented by:

$$\Delta G_{*COOH} = G_{*COOH} - G_{*} - G_{CO2} - G_{(H^+ + e^-)} \qquad (2)$$

$$\Delta G_{*CO} = G_{*CO} + G_{H2O} - G_{*} - G_{CO2} - 2 \times G_{(H^+ + e^-)} \qquad (3)$$

$$\Delta G_{*CHO} = G_{*CHO} + G_{H2O} - G_{*} - G_{CO2} - 3 \times G_{(H^+ + e^-)} \qquad (4)$$

$$\Delta G_{*CH2O} = G_{*CHO} + G_{H2O} - G_{*} - G_{CO2} - 4 \times G_{(H^+ + e^-)} \qquad (5)$$

$$\Delta G_{*CH3O} = G_{*CH3O} + G_{H2O} - G_{*} - G_{CO2} - 5 \times G_{(H^+ + e^-)} \qquad (6)$$

$$\Delta G_{*O} = G_{O*} + G_{CH4} + G_{H2O} - G_{*} - G_{CO2} - 6 \times G_{(H^{+} + e^{-})} \quad (7)$$

$$\Delta G_{*OH} = G_{*OH} + G_{CH4} + G_{H2O} - G_{*} - G_{CO2} - 7 \times G_{(H^{+} + e^{-})} \quad (8)$$

$$\Delta G_{(* + CH4 + 2H2O)} = G_{CH4} + 2 \times G_{H2O} - G_{CO2} - 8 \times G_{(H^{+} + e^{-})} \quad (9)$$

$$G_{(H^{+} + e^{-})} = 1/2\ G_{H2} - eU \quad (10)$$

where * is the surface of the catalysts, U is the applied overpotential, and e is the elementary charge. In this study, U = 0 V vs. RHE.

References

[1] Kresse, G.; Furthmüller, J., Efficiency of ab-initio total energy calculations for metals and semiconductors using a plane-wave basis set. Computational Materials Science 1996, 6 (1), 15-50.
[2] Kresse, G.; Furthmüller, J., Efficient iterative schemes for ab initio total-energy calculations using a plane-wave basis set. *Physical Review* B **1996**, 54 (16), 11169-11186.
[3] P.E. Blöchl, Projector augmented-wave method, P*hysical Review B*, **1994**,50 17953-17979
[4] Perdew, J. P.; Burke, K.; Ernzerhof, M. J. P. r. l., Generalized gradient approximation made simple. 1996, 77 (18), 3865.
[5] Grimme, S., Semiempirical GGA-type density functional constructed with a long-range dispersion correction. *J Comput Chem* **2006**, 27 (15), 1787-99.
[6] Henkelman, G. & Jónsson, H. Improved tangent estimate in the nudged elastic band method for finding minimum energy paths and saddle points. *The Journal of chemical physics* **2002**, 113, 9978-9985.
[7] Sheppard, D., Xiao, P., Chemelewski, W., Johnson, D. D. & Henkelman, G. A generalized solid-state nudged elastic band method. *The Journal of chemical physics* **2012**, 136, 074103.
[8] Henkelman, G., Uberuaga, B. P. & Jónsson, H. A climbing image nudged elastic band method for finding saddle points and minimum energy paths. *The Journal of chemical physics* **2000**, 113, 9901-9904.
[9] J. K. Nørskov*J. RossmeislA. LogadottirL. LindqvistJ. R. KitchinT. BligaardH. Jónsson. Origin of the Overpotential for Oxygen Reduction at a Fuel-Cell Cathode. *J. Phys. Chem. B* **2004**, 108, 46, 17886–17892.

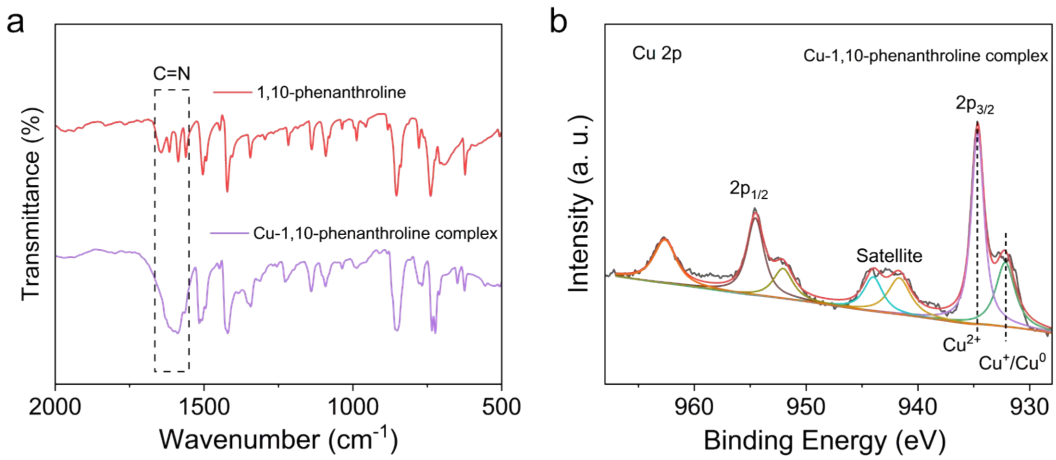

Fig. S1. (a) FTIR spectra of 1,10-phenanthroline and Cu-1,10-phenanthroline complex. (b) Cu 2p XPS spectrum of Cu-1,10-phenanthroline complex.

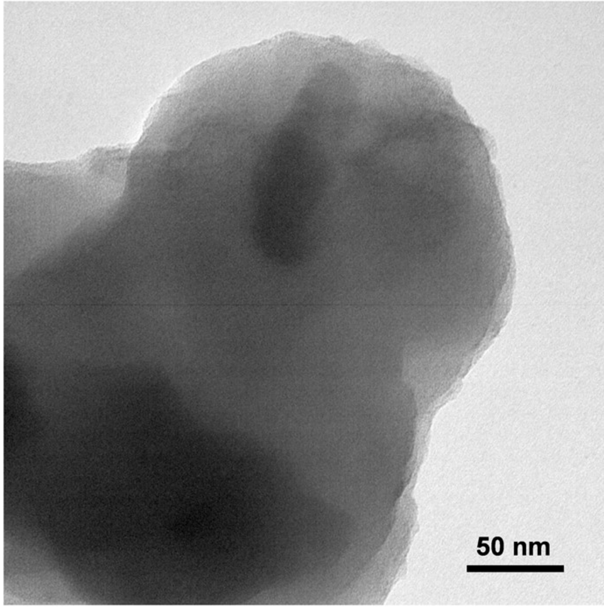

Fig. S2. TEM image of C_{60}.

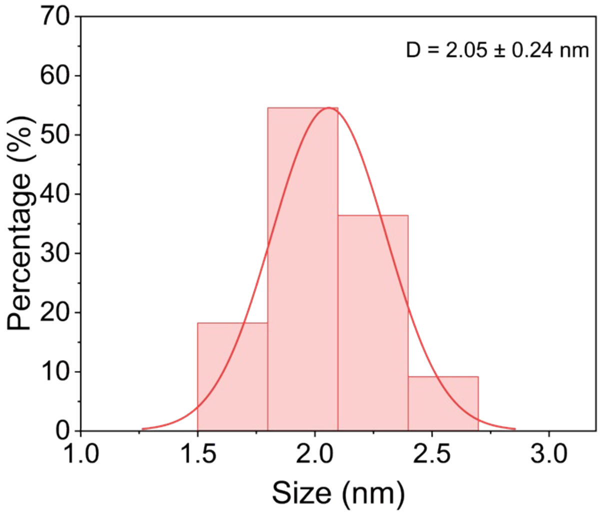

Fig. S3. Particle size distribution of copper clusters in p-Cu/C_{60}.

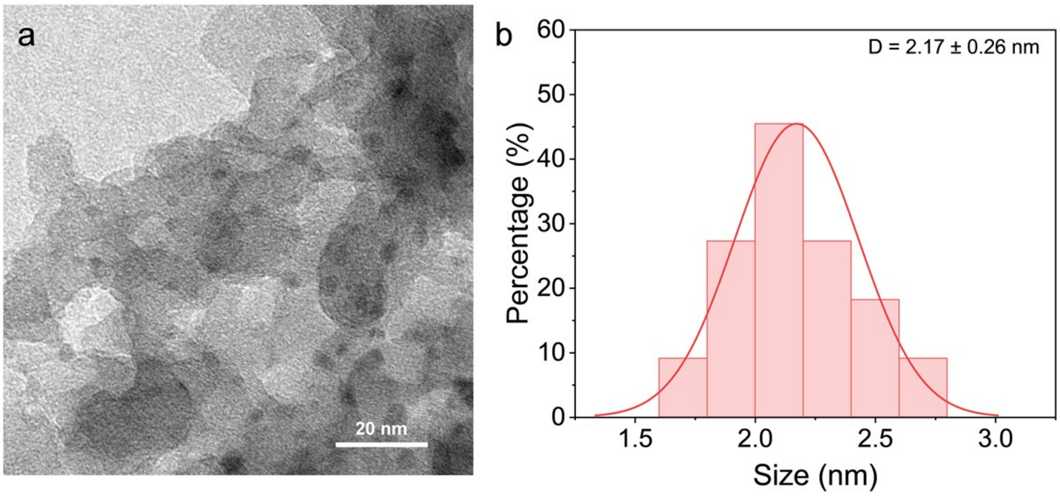

Fig. S4. (a) TEM image of p-Cu/CB. (b) Particle size distribution of copper clusters in p-Cu/CB.

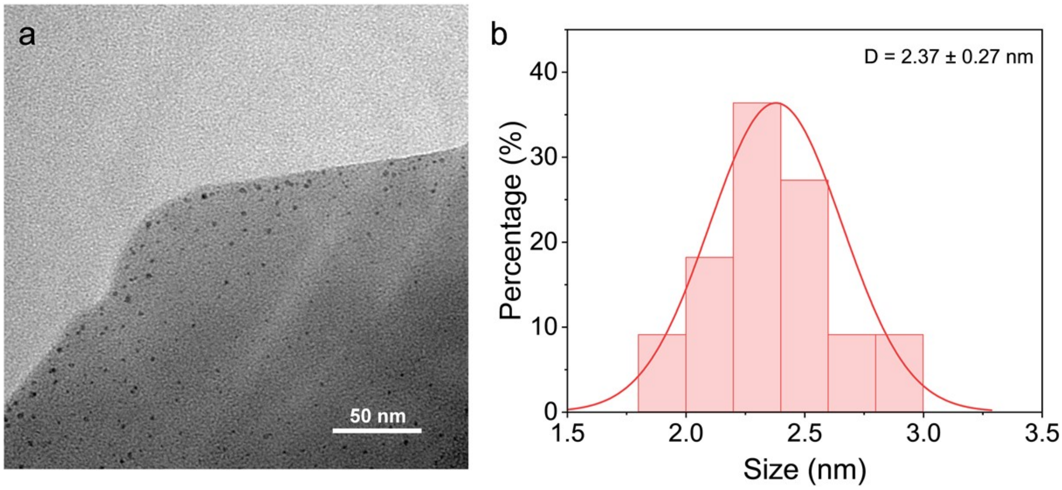

Fig. S5. (a) TEM image of Cu/C_{60}. (b) Particle size distribution of copper clusters in Cu/C_{60}.

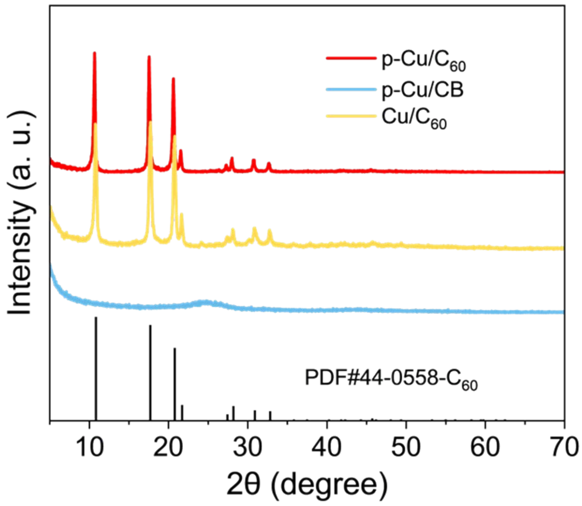

Fig. S6. PXRD spectra of p-Cu/C_{60}, p-Cu/CB and Cu/C_{60}.

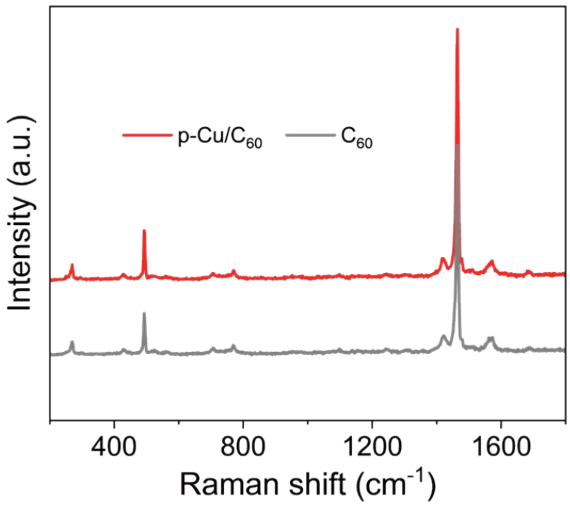

Fig. S7. Raman spectra of p-Cu/C_{60} and C_{60}.

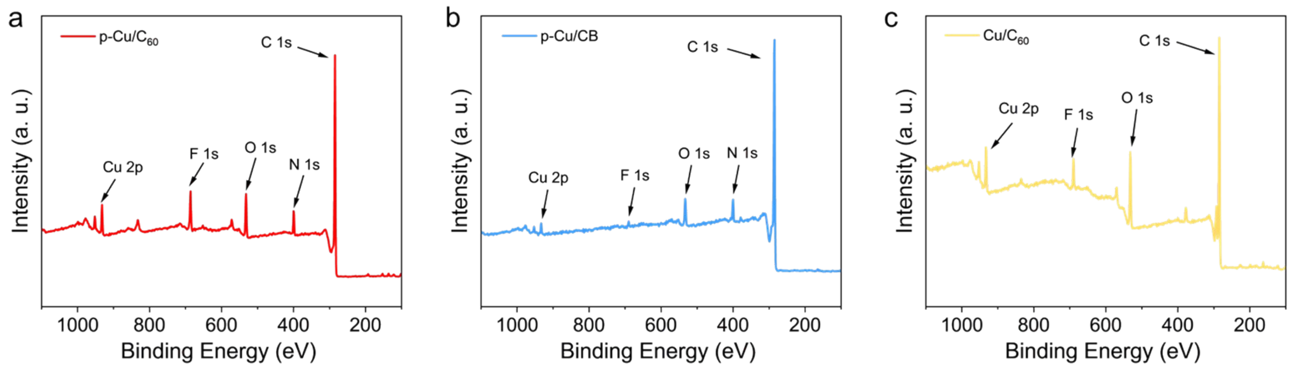

Fig. S8. XPS full survey spectra of p-Cu/C_{60} (a), p-Cu/CB (b) and Cu/C_{60} (c).

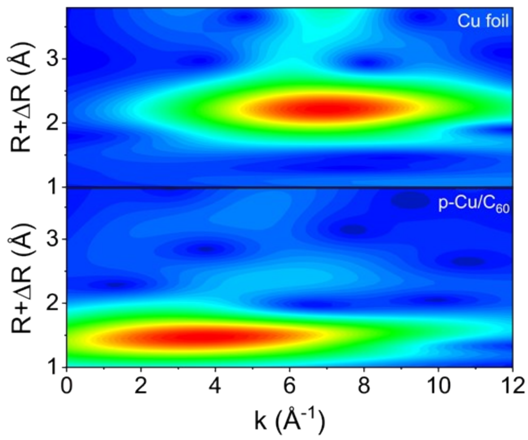

Fig. S9. Wavelet Transform results of p-Cu/C_{60} and Cu foil.

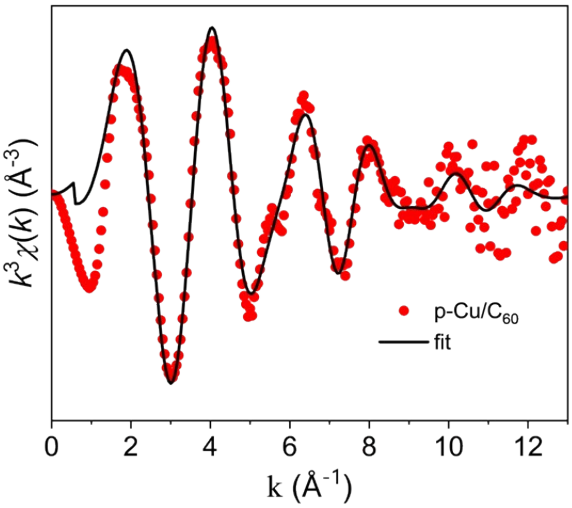

Fig. S10. EXAFS fitting result of p-Cu/C_{60} at k space.

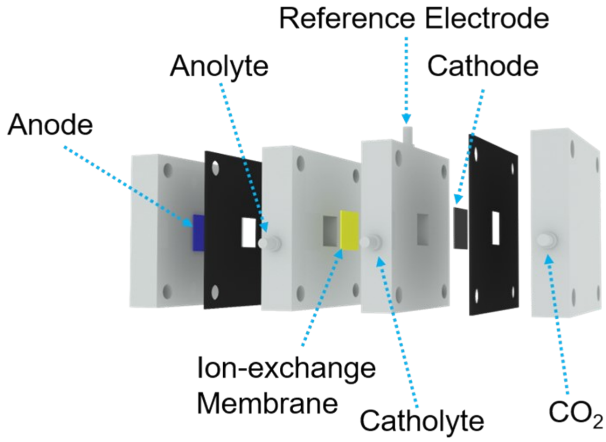

Fig. S11. Schematic of a gas-diffusion flow cell.

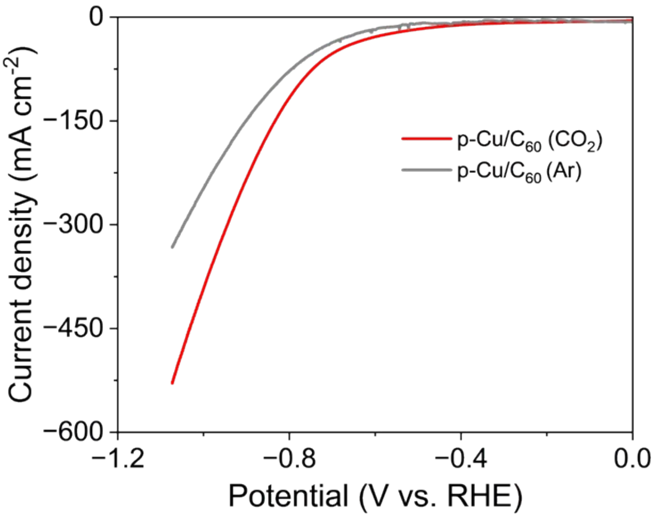

Fig. S12. LSV curves of p-Cu/C_{60} under Ar and CO_2.

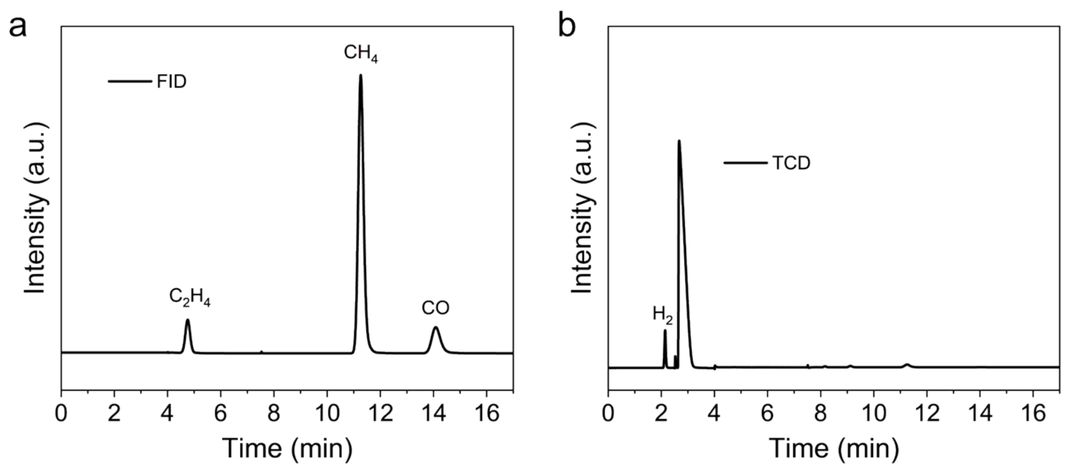

Fig. S13. GC profiles during CO_2 reduction electrolysis at 250 mA cm^{-2} using p-Cu/C_{60}.

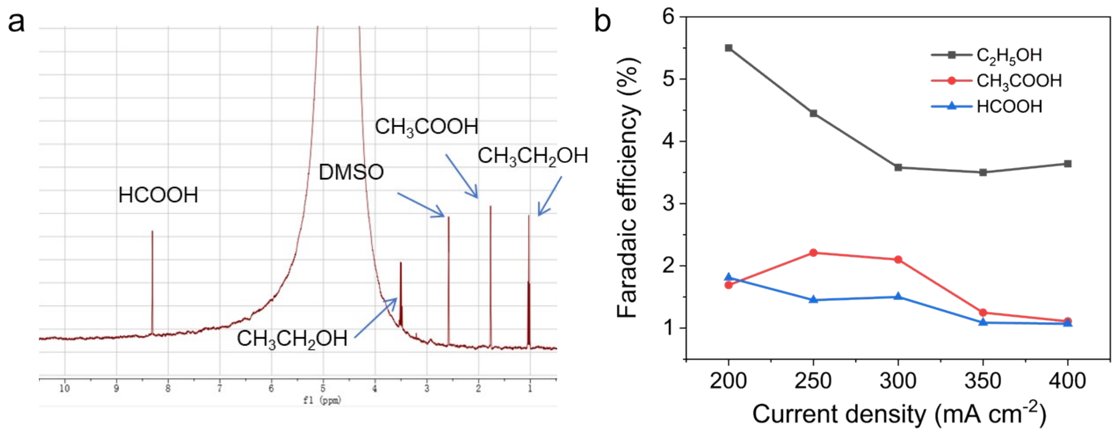

Fig. S14. (a) ^{1}H NMR spectrum after CO_2 reduction electrolysis at 350 mA cm^{-2} using p-Cu/C_{60}. (b) Faradaic efficiency of the liquid products.

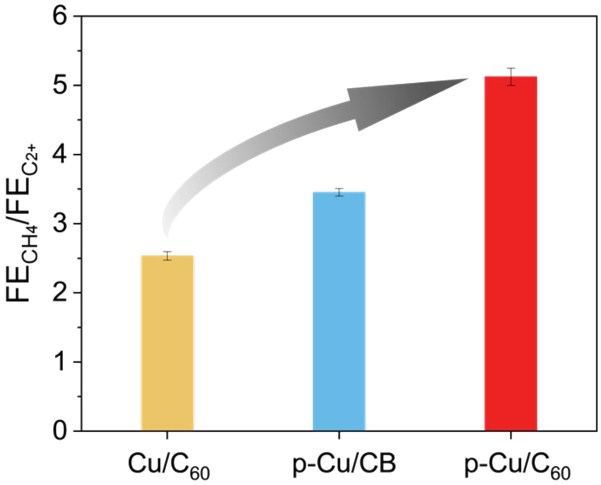

Fig. S15. The ratio of CH_4 Faradaic efficiency to C_{2+} Faradaic efficiency on p-Cu/C_{60}, p-Cu/CB and Cu/C_{60} at 350 mA cm^{-2}.

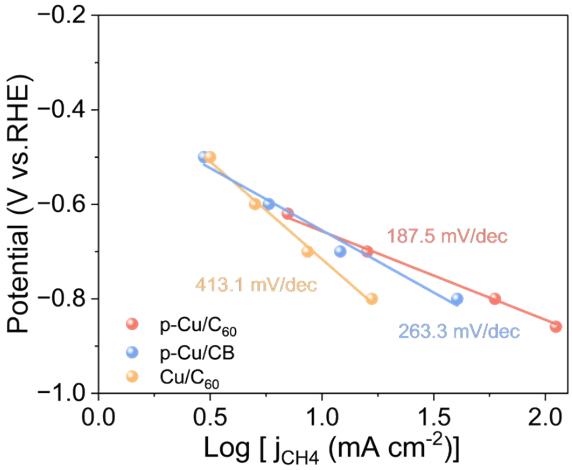

Fig. S16. Tafel plots of p-Cu/C_{60}, p-Cu/CB and Cu/C_{60}.

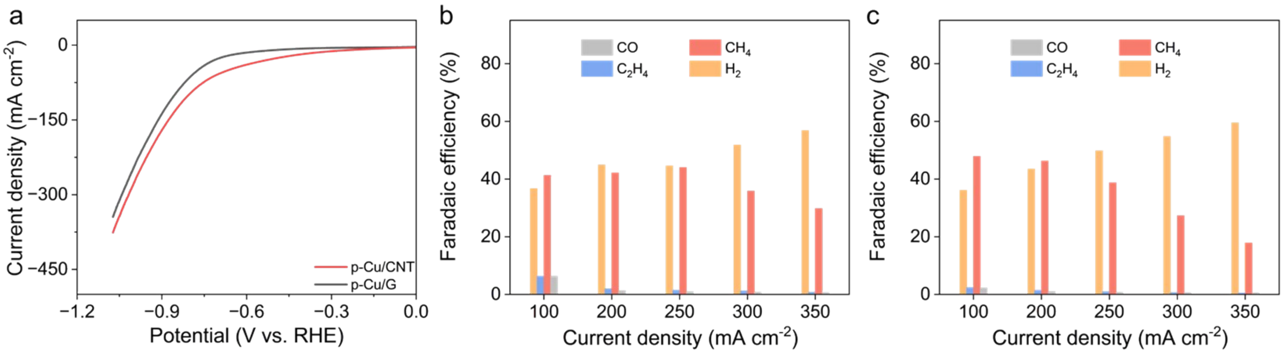

Fig. S17. (a) LSV curves of p-Cu/G and p-Cu/CNT. (b, c) Faradaic efficiency of p-Cu/G (b) and p-Cu/CNT (c).

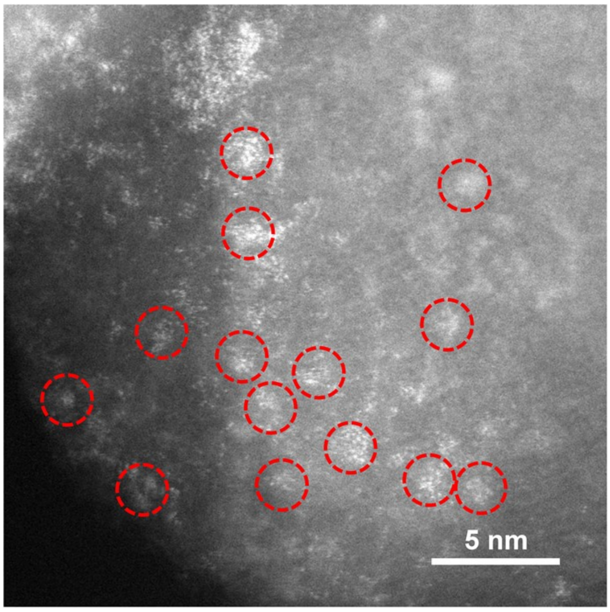

Fig. S18. Aberration-corrected HAADF-STEM image of p-Cu/C_{60} after stability test.

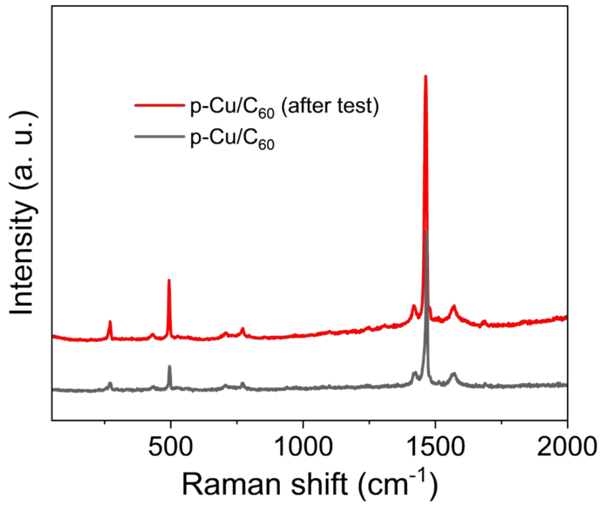

Fig. S19. Raman spectra of p-Cu/C_{60} before and after stability test.

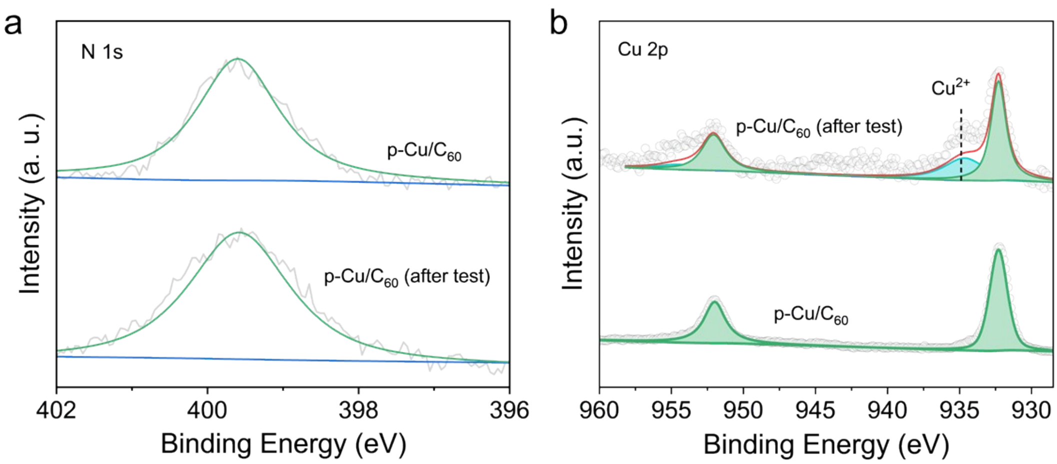

Fig. S20. (a) N 1s and (b) Cu 2p XPS spectra of p-Cu/C_{60} before and after stability test.

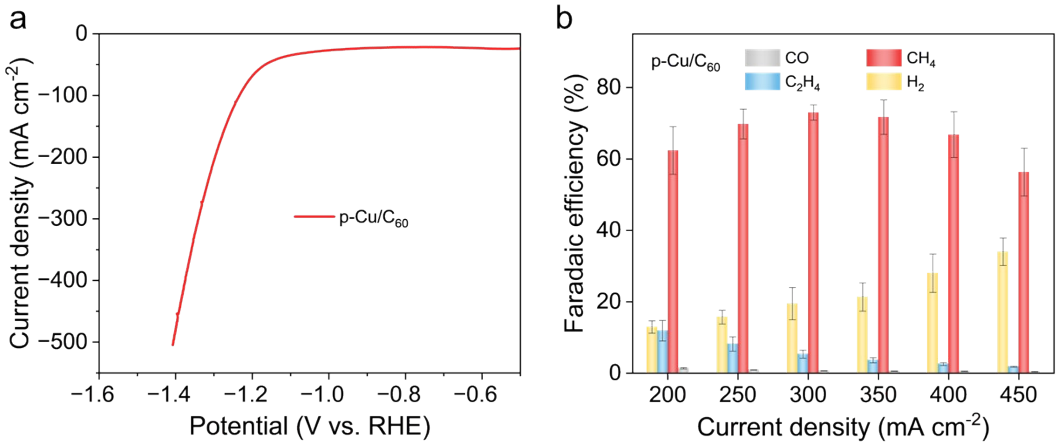

Fig. S21. (a) LSV curve (b) Faradaic efficiency of p-Cu/C_{60} in acidic electrolyte (0.05M H_2SO_4 + 1M KCl).

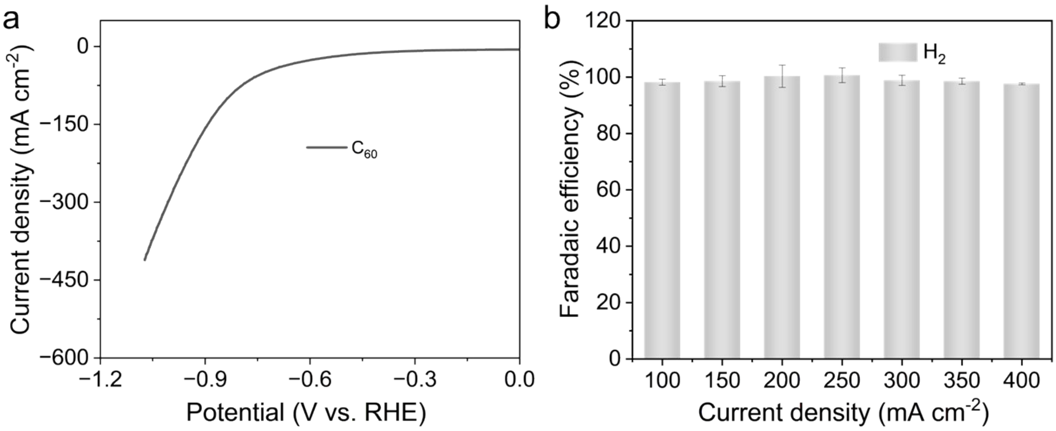

Fig. S22. (a) LSV curve (b) H_2 Faradaic efficiency of C_{60}.

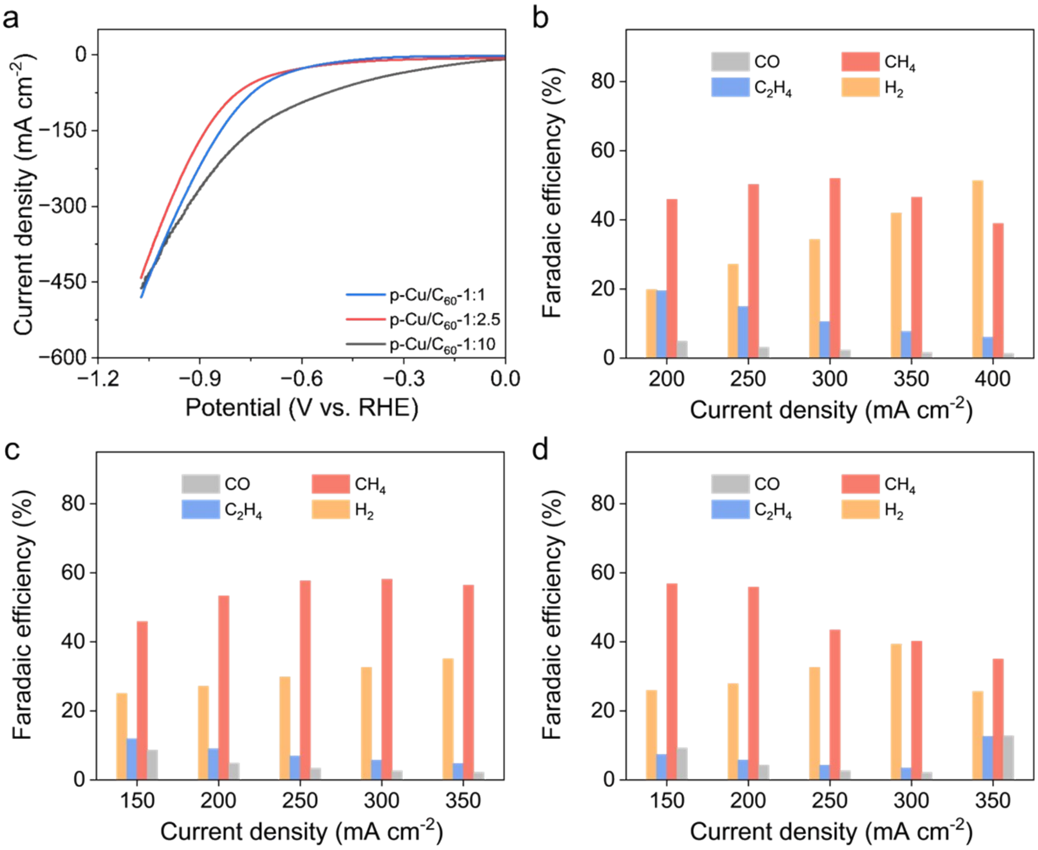

Fig. S23. (a) LSV curves of the catalysts with different precursor ratios. (b-d) Faradaic efficiency of p-Cu/C$_{60}$-1:1 (b), p-Cu/C$_{60}$-1:2.5 (c) and p-Cu/C$_{60}$-1:10 (d).

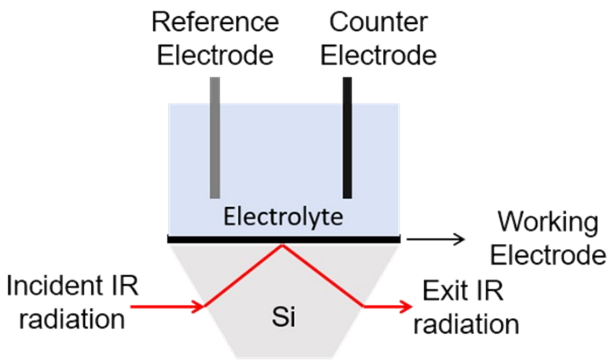

Fig. S24. Schematic of *in situ* ATR-IR experiments.

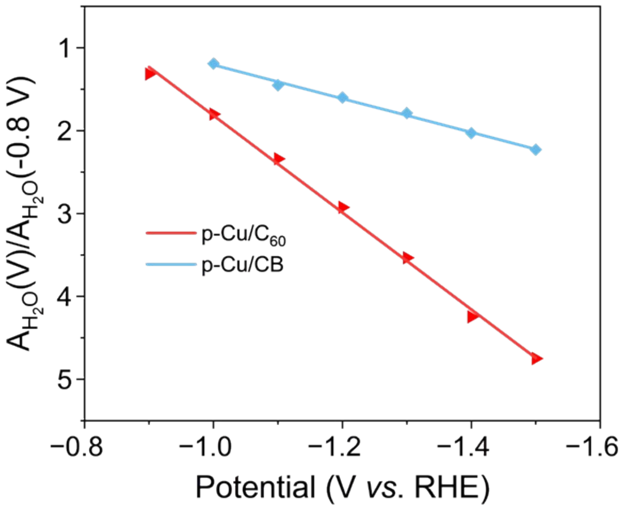

Fig. S25. The water consumption calculated from water peak area in the *in situ* ATR-IR spectra of p-Cu/C_{60} and p-Cu/CB.

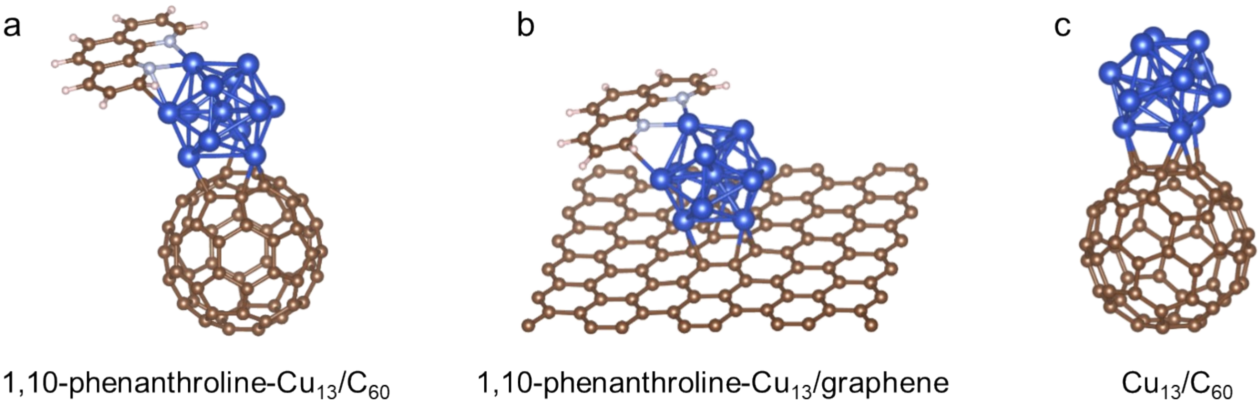

Fig. S26. Theoretical calculation structure models of 1,10-phenanthroline-Cu_{13}/C_{60} (a), 1,10-phenanthroline-Cu_{13}/graphene (b) and Cu_{13}/C_{60} (c).

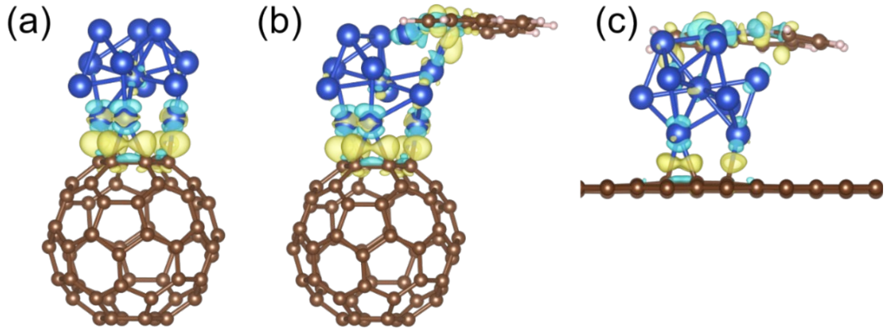

Fig. S27. Side views of the charge density difference between the Cu_{13} cluster and the C_{60}/graphene/1,10-phenanthroline on Cu_{13}/C_{60} (a), 1,10-phenanthroline-Cu_{13}/C_{60} (b), and 1,10-phenanthroline-Cu_{13}/graphene (c). The isosurface level is set to 0.005 e/Å^3. Yellow and blue areas represent the accumulation and depletion of electron, respectively.

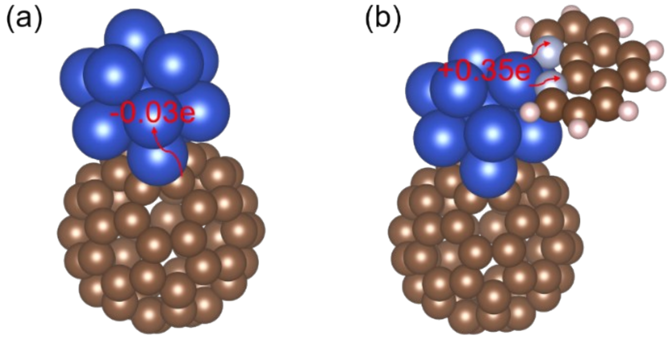

Fig. S28. The calculated Bader charge on the Cu active site of Cu_{13}/C_{60} (a), and 1,10-phenanthroline-Cu_{13}/C_{60} (b).

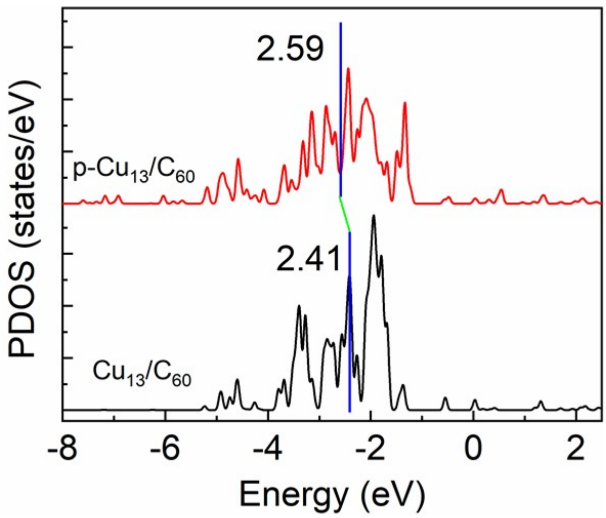

Fig. S29. The calculated partial density of states of the Cu d states for 1,10-phenanthroline-Cu_{13}/C_{60} and Cu_{13}/C_{60}. The blue lines refer to the d band centers of Cu atoms. The Fermi-level energy was set to zero.

Tab. S1. Structural parameters of EXAFS fitting for p-Cu/C_{60}.

Sample	Scattering path	R (Å) [a]	C.N. [b]	σ^2 [c]	ΔE_0 (eV)[d]
p-Cu/C_{60}	Cu-N/C	2.01	3.1	0.008	1.2
	Cu-Cu	2.85	1.2	0.010	-5.8

a: bond distance; b: coordination number; c: Debye-waller factors; d: the inner potential correction. The data ranges are presented as $2.7 \le k \le 11$ Å^{-1}, $1 \le R \le 2.8$ Å. Error bounds that characterize the structural parameters obtained by EXAFS spectroscopy were estimated as CN ± 20%: σ^2 ± 20%: R ± 0.03 Å

Tab. S2. Summary of some recently reported CO_2-to-CH_4 conversion electrocatalysts.

	Catalyst	Electrolyte	CH_4 maximum faradaic efficiency (%)	Maximum J_{CH_4} (mA/cm^2)	Reference
1	Cu/ceria-H_2	1 M KOH	70.03	105	Angew. Chem. Int. Ed. 2025, 64, e202415642
2	3,5-diamino-1,2,4-triaz	1 M KOH	52	130	Nature Energy. 2024, 9, 1397
3	Cu_{38}	1 M KOH	27.98	42.8	J. Am. Chem. Soc. 2024, 146, 28131
4	N-aGQDs-A9	1 M KOH	63	258	Adv. Mater. 2022, 34, 2105690
5	Cu-PTI	1 M KOH	68	348	Adv. Mater. 2024, 36, 2300713
6	Cu SAs/HGDY	1 M KOH	72.1	230.7	Angew. Chem. Int. Ed. 2023, 62, e202314121
7	Cu-I	1 M KOH	57.2	60.7	Adv. Funct. Mater. 2022, 32, 2203677
8	Cu-Ce-Ox	1 M KOH	67.8	135.6	J. Am. Chem. Soc. 2022, 144 , 2079
9	PDA@ER-Cu	1 M KOH	60	125.6	Adv. Funct. Mater. 2025, 35, 2420881
10	Cu/C	1 M KOH	61.7	153.7	ACS Catalysis. 2022, 12, 8252
11	CuNCP	1 M KOH	60	170	Angew. Chem. Int. Ed. 2024, 63, e202315922
12	Cu-PtNPs	1 M KOH	70.4	140.8	Angew. Chem. Int. Ed. 2025, 64, e202424749
13	p-Cu/C_{60}	1 M KOH	68	255	This Work
14	Ag@SiO2 -8 h	0.5 M K_2SO_4 + 0.05 M H_2SO_4	56.6	132.6	Adv. Funct. Mater. 2025, 35, 2503126
15	PtNPs@Th	0.1 M HCl+0.5 M KCl	23	~7	Natl. Sci. Rev. 2024, 11, nwae361
16	EDTA/CuPc/CNP	0.005 M H_2SO_4	71	71	Nature Commun. 2023, 14, 3314
17	p-Cu/C_{60}	0.05 M H_2SO_4+1 M KCl	72	264	This Work